Modelling the adsorption of proteins to nanoparticles at the solid-liquid interface

Mikhail Soloviev,[a] Giuliano Siligardi,[b] Danilo Roccatano[c] and Enrico Ferrari[†d]

[a] Department of Biological Sciences, Royal Holloway University of London, Egham TW20 0EX, UK.

[b] Diamond Light Source, Diamond House, Chilton, Didcot OX11 0DE, UK.

[c] School of Mathematics and Physics, University of Lincoln, Lincoln LN6 7TS, UK.

[d] School of Life Sciences, University of Lincoln, Lincoln LN6 7TS, UK.

† Corresponding author:

Enrico Ferrari

School of Life Sciences, University of Lincoln, Brayford Pool, Lincoln LN6 7TS, UK

email: eferrari@lincoln.ac.uk; phone: +44 (0) 1522 886302

Abstract

Hypothesis

We developed a geometrical model to determine the theoretical maximum number of proteins that can pack as a monolayer surrounding a spherical nanoparticle. We applied our new model to study the adsorption of receptor binding domain (RBD) of the SARS-CoV-2 spike protein to silica nanoparticles. Due to its abundance and extensive use in manufacturing, silica represents a reservoir where the virus can accumulate. It is therefore important to study the adsorption and the persistence of viral components on inanimate surfaces.

Experiments

We used previously published datasets of nanoparticle-adsorbed proteins to validate the new model. We then used integrated experimental methods and Molecular Dynamics (MD) simulations to characterise binding of the RBD to silica nanoparticles and the effect of such binding on RBD structure.

Findings

The new model showed excellent fit with existing datasets and, combined to new RBD-silica nanoparticles binding data, revealed a surface occupancy of 32% with respect to the maximum RBD packing theoretically achievable. Up to 25% of RBD's secondary structures undergo conformational changes as a consequence of adsorption onto silica nanoparticles.

Our findings will help developing a better understanding of the principles governing interaction of proteins with surfaces and can contribute to control the spread of SARS-CoV-2 through contaminated objects.

Keywords

Protein corona, protein adsorption, silica nanoparticles, SARS-CoV-2, coronavirus, sphere packing

1. Introduction

Studies of protein adsorption at the solid-liquid interface are complicated by the extreme diversity of proteins, and a model applicable to any protein-material pair remains elusive [1]. Previously reported methods to predict the maximum number of molecules adsorbed to nanoparticles relied on estimations of the surface area of spherical nanoparticles, further extended by the radius of the globular protein, and the cross-section of the protein [2]. Other studies assumed a fixed value of 0.65 as a fractional protein volume occupancy inside a spherical protein corona surrounding the nanoparticle [3]. Weaknesses of previously published models emanate from the assumption of a

44 uniform protein packing density irrespective of the size of the protein relative to the nanoparticle. The
45 ability to accurately model and predict the maximum packing density of molecules on surfaces is
46 required to achieve better understanding of the principles governing interaction of biological
47 molecules with solid interfaces and will contribute to the development of composite or designer
48 materials.

49

50 From the experimental point of view, the use of nanoparticles, rather than bulk materials, is a
51 promising approach to broaden the knowledge of protein-material interactions [4], as long as the
52 materials of interest are available as colloids. The large surface area of colloidal suspensions, enables
53 biochemical and biophysical methods that would otherwise have insufficient sensitivity when
54 performed on bulk materials, especially when the amount of protein is limited. The development of
55 small-scale, fast and accessible methods to investigate protein adsorption on nanoparticles may be
56 the key to address the large biochemical and structural diversity of proteins and eventually could
57 provide sufficient data to generate a predictive model of protein-material interactions.

58

59 Whilst the main route of transmission of the SARS-CoV-2 virus is thought to be via aerosol droplets,
60 these could also deposit on solid surfaces and be later picked up on contact with the affected surface.
61 Previously published studies assessed the infection rate and persistence of SARS-CoV-2 on various
62 solid surfaces such as cardboard, plastic, steel and copper surfaces using cell cultures [5], That, and
63 other similar studies of related coronaviruses [6,7], provided useful observations that can inform the
64 use of ordinary materials during a coronavirus pandemic, potentially limiting transmission via
65 contaminated surfaces. Past studies also highlighted that different inanimate surfaces are associated
66 with very different virus persistence, spanning from a few hours to 28 days [7], depending on the exact
67 nature of the materials on which the coronavirus particles were adsorbed. For example, evidence
68 shows that SARS-CoV-1 and SARS-CoV-2 may survive for 4-8 hours on copper [5], whereas the viruses

69 remain infective on glass, paper, plastic and other metals up to 5 days after initial exposure [6]. Under
70 certain environmental conditions, other coronaviruses, such as Middle East Respiratory Syndrome
71 (MERS) coronavirus, Transmissible Gastroenteritis Virus (TGEV) and Mouse Hepatitis Virus (MHV),
72 were found to be infective even 28 days after inoculation on steel [7], but the mechanisms that
73 determine such a broad material-specific response remain unexplored. It is likely that the persistence
74 of infective viral particles at the solid-liquid and solid-air interface is determined by a combination of
75 environmental factors (e.g., temperature and exposure to light), structure and biochemistry of the
76 viral biomolecules at the interface, primarily the exposed spike proteins and the physicochemical
77 nature of the material interface [8–10].

78

79 Having developed a mathematical approach to describe protein packing on nanoparticles, we used it
80 to study the interaction between silica and the highly exposed targeting moiety of SARS-CoV-2 spike
81 glycoprotein receptor binding domain (RBD). RBD domain of the SARS-CoV-2 spike protein is
82 responsible for targeting the virus to human epithelial cells via high affinity interaction with
83 Angiotensin-Converting Enzyme 2 (ACE2) receptor. Silica nanoparticles (SiO_2 NPs) were used to model
84 silica material such as glass, where silica is a major constituent. The dissociation constant (K_D) of RBD-
85 SiO_2 NPs and the maximum protein load (L_{max}) were determined under physiological conditions (Figure
86 1A). Taking advantage of the spherical shape of the SiO_2 NPs and the globular structure of the RBD, a
87 general geometrical model was proposed to compare the measured density of adsorbed proteins with
88 the theoretical maximum achievable packing (Figure 1B). Molecular Dynamics (MD) simulations were
89 used to evaluate the likely orientation of the RBD on silica and identify the amino acid residues in
90 closest contact with the silica surface (Figure 1C). Circular Dichroism (CD) was used to study changes
91 in the secondary structure of RBD upon adsorption on SiO_2 NPs (Figure 1D). This integrated approach
92 can be applied in the quest to find safe materials to use during a coronavirus pandemic. The methods

can be also potentially applied to other protein-material interfaces to broaden the understanding of the general principles of protein adsorption on solid surfaces.

2. Materials and Methods

Geometrical model

The maximum number of protein molecules that can be regularly packed on a spherical nanoparticle N_{max} was calculated from equation 1, assuming the protein's shape is approximated to a sphere. Equation 1 was obtained by maximising the number of equidistant points surrounding a sphere and assuming that those points are at the centre of adjacent spherical proteins packed according to a near-hexagonal pattern [11]. Details of the geometrical model and the limits of its validity are presented in the Supplementary Methods.

$$N_{max} = \left\lfloor \frac{2\sqrt{3}}{3}\pi\frac{1}{\alpha^2} \right\rfloor \qquad \text{(equation 1)}$$

Here, α represents half the angular distance between two adjacent spherical proteins on the nanoparticle, as outlined in Supplementary Figure 1. The radius of the spherical protein R_2 and the radius of the spherical nanoparticle R_1 (with $R_2/R_1 = r$) allow to calculate the $\sin\alpha$:

$$\sin\alpha = \frac{R_2}{R_1+R_2} = \frac{r}{1+r} \qquad \text{(equation 2)}$$

The comparison between the new geometrical model described by equations 1 and 2 and a previous geometrical model informed by scattering experiments on microemulsions is detailed in the Supplementary Methods.

The radius R_2 of the sphere that best approximates the size of any globular protein was calculated using equation 3 as previously described [12].

$$R_2 = \sqrt[3]{\frac{3}{4\pi}\frac{\bar{v}M_r}{N_A}10^{21}} = 0.066\sqrt[3]{M_r} \qquad \text{(equation 3)}$$

115 Equation 3 gives the radius of a spherical protein in nm units and assumes proteins as spheres
116 characterised by a partial specific volume $\bar{v}$ ($cm^3\ g^{-1}$) and a mass (g), that is the ratio between the
117 relative mass M_r ($g\ mol^{-1}$) and the Avogadro's constant N_A (mol^{-1}). To simplify equation 3 further, the
118 partial specific volume of all the proteins considered was set at an average value of 0.73 $cm^3\ g^{-1}$ as
119 previously described [12].

120 Binding assay

121 Recombinant SARS-CoV-2 Spike Protein RBD expressed in HEK293 Cells, comprising amino acids 319-
122 541 and a C-terminal His Tag, was purchased from Sino Biological (>95% purity). The protein was mixed
123 with a set of serially diluted 50 nm plain silica nanoparticles (Polysciences) in 100 mM sodium
124 phosphate buffer, pH 7.0. The final concentration of RBD was $[C]_0$ = 0.150 mg mL^{-1} in all solutions,
125 whereas the concentration of nanoparticles [NP] ranged from 0 to 15 mg mL^{-1}. The solutions were
126 incubated for 2 hours at 20°C to allow adsorption of the RBD onto the nanoparticles. Following
127 incubation 30 µL of the solutions were centrifuged at 7,000 g for 20 minutes at 20°C. The supernatants
128 were collected and the unbound protein concentration [C] of each solution was determined using
129 Bradford assay. For each solution, the nanoparticle-bound protein concentration $[C]_{NP}$ was
130 determined by subtraction of [C] from the initial concentration $[C]_0$ and plotted versus the
131 nanoparticle concentration [NP] and residual concentration of the solution [C], according to the Hill-
132 Langmuir equation (equation 4).

133 $$[C]_{NP} = [C]_0 - [C] = L_{\max}[NP]\frac{[C]}{K_D+[C]} \qquad \text{(equation 4)}$$

134 The parameters L_{max} (mg of protein per mg of silica) and K_D (dissociation constant) of equation 4 were
135 determined using non-linear least squares fitting of the experimental data to a re-arranged equation
136 4 (see supplementary equation 7 in the Supplementary Methods). The K_D obtained in mg mL^{-1} units
137 was converted into nM using a relative mas M_r of 35,000 g mol^{-1}, as indicated by the supplier of the
138 RBD. The number of bound RBD molecules per nanoparticle at equilibrium was calculated from the
139 experimentally determined L_{max}:

140 $$N = L_{\max}\frac{4\pi}{3}R_1^3\rho\frac{N_A}{M_r}10^{-21} \qquad \text{(equation 5)}$$

141 Equation 5 calculates the number of proteins adsorbed per particle (N) from the measured protein
142 load, using the measured mass of bound protein and the calculated mass of an individual nanoparticle
143 as detailed in the Supplementary Methods. A nanoparticle with radius R_1 = 25 nm and a density ρ of
144 2.0 g cm^{-3} was based on the manufacturer's specification. To estimate the percentage of binding
145 compared to the maximum theoretical packing, N was divided by N_{max} obtained from the geometrical
146 model.

147 Molecular dynamics

148 The initial atomic coordinates of the RBD were obtained from the electron microscopy structure model
149 of the complex between the RBD and ACE2 [13]. The structure is deposited in the Protein Data Bank
150 with the PDB ID 6M17. The system was prepared for MD simulations using the web-tool CHARMM-
151 GUI [14,15] and GROMACS software (version 2020). The protein structure was protonated according
152 to the experimental pH=7.0, yielding a net +2 charge. The surface of the nanoparticle was represented
153 as an 11x11x2.5 nm planar slab of silica atoms. 13.3% of the hydroxyl groups (159 in total) on the silica
154 surface were deprotonated and neutralised using sodium counter ions [16]. The silica slab was
155 enclosed in a rectangular box of 11x11x14 nm that was filled with approximately 40,450 water
156 molecules using the TIP3P model [17]. Sodium (265 atoms) and chloride (108 atoms) counter-ions
157 were also added to obtain an ionic strength comparable to the experimental one. The RBD was placed
158 in the centre of the simulation box at approximately 4 nm from the silica surface. Three independent
159 MD simulations with three orthogonal initial orientations reported in Supplementary Figure 2 were
160 performed for 100 ns each with an integration time of 2 fs. The force field from CHARMM (version 36)
161 was used for the interaction parameters [18] and the parameters of silica oxide atoms generated with
162 CHARMM-GUI were based on previously reported values [16]. The MD simulations were carried out
163 at constant temperature and pressure. Initial velocities for each atom were generated from the
164 Maxwell distribution at 298.15 K. The temperature was kept constant at 298.15 K using the Nose-

165 Hoover thermostat with a coupling constant of 1 ps [19]. The pressure was maintained constant at 1
166 bar using Parrinello-Rahman isotropic barostat [20,21] with a coupling constant of 5 ps. The bond-
167 lengths of hydrogen atoms were constrained using the LINCS algorithm [22]. The SETTLE algorithm
168 was used to constrain bond lengths and bond angles of water molecules [23]. Electrostatic interactions
169 were evaluated using particle mesh Ewald method with a real space cut-off of 1.2 nm, grid spacing of
170 0.12 nm and fourth-order spline interpolation [24]. Lennard-Jones interactions were truncated at 1.2
171 nm, and the pair-list was updated every 20 time-steps. All the systems were energy minimized for at
172 least 1000 steps using the steepest descents method in order to remove any short distance clashes of
173 the atoms in the generated solvent molecules. Subsequently, the density of the system was allowed
174 to adjust to the equilibrium value by performing MD with position restraints only on the protein heavy-
175 atoms.

176 Calculations of Poisson–Boltzmann electrostatics were conducted using the Adaptive Poisson-
177 Boltzmann Solver (APBS) server and the RBD structure PDB ID 6M17 [25,26]. The structure was pre-
178 processed using the PDB2PQR server to estimate titration states of the ionizable residues at pH=7.0
179 [26,27]. The electrochemical potential at the surface of RBD was represented by superimposing the
180 obtained electrochemical field to the surface of RBD using the software UCSF Chimera [28].

181 Circular Dichroism

182 The near-UV and near-CD of a RBD solution in 100 mM sodium phosphate, pH=7.0, were acquired with
183 a 1 cm pathlength and 2x1 mm aperture using B23 beamline module A (Diamond Light Source) with
184 highly collimated microbeam. Bandwidth was 1.1 nm, and the integration time was 2 seconds. The
185 measurements were conducted in quadruplicate. The protein concentration in mg mL^{-1} was
186 calculated from Beer-Lambert's law using the absorbance at 280 nm and calculated extinction
187 coefficient of 33,500 $M^{-1}cm^{-1}$, based on 2 tryptophan (2 x 5,500 $M^{-1}cm^{-1}$) and 15 tyrosine residues (15
188 x 1500 $M^{-1}cm^{-1}$). UV and CD spectra in the 180-300 nm region were acquired from the RBD solution in
189 the presence of 16 mg mL^{-1} silica nanoparticles as well as the residual RBD remaining in solution after

190 the removal of nanoparticles by centrifugation (see details of preparation in the binding assay section).
191 The spectra were measured with a Chirascan Plus using a Hellma cylindrical cuvette of 0.02 cm
192 pathlength. Bandwidth was 1 nm, and the integration time was 2 seconds. The measurements were
193 conducted in quadruplicate. UV extinction and CD spectra of RBD bound to silica nanoparticles were
194 obtained by subtracting the spectra before and after the removal of nanoparticles. The spectra were
195 corrected for the light scattering contribution due to nanoparticles. The light scattering correction of
196 UV extinction spectra was conducted using the software a|e - UV-Vis-IR Spectral Software 1.2,
197 (FluorTools). The light scattering correction for CD spectra was obtained by identifying the spectral
198 contribution from two samples containing the same amount of RBD and nanoparticle concentrations
199 of 8 and 16 mg mL^{-1} respectively, thus exhibiting different degrees of light scattering. As the spectral
200 tails in the 300-250 nm region of the CD spectra do not have detectable protein spectral contribution,
201 they were superimposed to determine the multiplying factor due to light scattering. This judicious
202 approximation to correct the CD spectra from light scattering and the normalisation of the protein
203 concentration obtained from UV extinction spectra (Supplementary Figure 5) were used to determine
204 whether the SiO_2 nanoparticles were perturbing the protein folding of the bound RBD protein. The CD
205 data analysis was conducted using B23 CDApps suite of programs [29]. The secondary structure
206 estimation (SSE) from CD data of RBD in solution and silica-bound RBD with subtracted light scattering
207 was conducted using ContinLL algorithm with various base sets of soluble proteins (SP) (SP37, SP43,
208 SP48 and SP56) choosing the results with the lowest standard deviation [30].

209

210 3. Results

211 Development of a protein packing model

212 We developed a geometrical model to determine the theoretical maximum number of proteins that
213 can pack as a monolayer surrounding a nanoparticle. The model is based on the assumption that the
214 nanoparticle is a sphere of radius R_1 and that the overall shape of the surrounding protein molecules

215 can be also approximated to identical spheres with radius $R_2 < R_1$ (Supplementary Figure 1). The
216 maximum number of packed spheres (N_{max}) is obtained by projecting a near-regular hexagonal tiling
217 onto the nanoparticle and is given by equation 1 (see Materials and Methods). In this new model, N_{max}
218 depends on the ratio R_2/R_1. Examples of N_{max} and their visual representation for various R_2/R_1 are given
219 in Figure 2A. To determine the radius R_2 of the sphere that best describes the size of a given globular
220 protein, we employed equation 3 (see Materials and Methods), which uses the relative mass of the
221 protein (M_r) to calculate the approximate radius [12].

222 An existing dataset of globular proteins spanning a broad range of M_r (5.8 to 250 kDa) was used to
223 validate the new geometrical model (Figure 2B). Those data were based on experimental
224 measurements of the number of protein molecules bound per gold nanoparticles of radius R_1=7.5 nm
225 under conditions that maximised the packing and retention of proteins onto the gold surface [31]. The
226 theoretical N_{max} calculated from equations 1 and 3, matches the experimental data very well with
227 coefficient of determination R^2 of 0.962 (Figure 2B). The size of the globular proteins included in the
228 dataset [31] spans a range of R_2/R_1 from 0.16 (Insulin) up to 0.56 (Catalase), which is within the validity
229 range of the model ($R_2/R_1 \leq 0.6$, see Supplementary Methods).

230 Together these results suggest that the new geometrical model can be used to predict the theoretical
231 N_{max}, based on the M_r of a given globular protein. In situations other than the ideal gold nanoparticle
232 system described above, for example when using non-ideal adsorption conditions, the model can be
233 used to define the surface occupancy N/N_{max}, which is the fraction of the available packing space
234 effectively occupied by protein molecules under the specific conditions used. The surface occupancy
235 is likely to depend on protein-material pairs, with materials like silica nanoparticles possibly showing
236 more sparse binding than gold, as silica does not form covalent bonds with any amino acid side chains,
237 resulting in weaker and reversible binding.

238 Adsorption of SARS-CoV-2 RBD onto silica nanoparticles

239 The surface occupancy of silica-bound SARS-CoV-2 RBD was determined by measuring the maximum
240 protein load (L_{max}) of RBD on SiO_2 NPs. Different concentrations of nanoparticles were titrated into
241 RBD solutions with identical initial concentration of the protein. Bound and unbound protein were
242 then separated and their concentration determined. The data in Figure 3 were fitted to equation 4
243 (see Experimental section) and yielded a L_{max} of 80.9 ± 6.9 μg mg^{-1} (μg of protein per mg of silica) and
244 K_D of 13.3 ± 5.0 μg mL^{-1},with the estimated intervals represented by standard errors. 13.3 μg mL^{-1} of
245 RBD equates 380 nM, suggesting a relatively low affinity of RBD to silica. It is important to point out
246 that each SARS-CoV-2 virion presents an average of 26 ± 15 spike proteins, each having three copies
247 of the RBD [32]. Although not all RBDs will be correctly oriented, it is likely that they can cooperatively
248 interact with the silica surface and increase the overall binding affinity substantially. A value N=182
249 was calculated from the measured L_{max} using equation 5 for monodispersed nanoparticles of R_1=25
250 nm (see Experimental section), whereas a R_2 of 2.16 nm and N_{max} of 570 were calculated from equation
251 3 and 1 respectively. The resulting surface occupancy N/N_{max} of 32% suggests sparse adsorption rather
252 than dense packing, as also illustrated in the inset of Figure 3.

253 MD simulations of SARS-CoV-2 RBD interaction with silica nanoparticles

254 RBD accounts for approximately 17% of a single full-length spike protein. We therefore went on to
255 identify the likely contact interface between the RBD and silica and whether that interface is normally
256 exposed on the spike protein or whether it becomes available only as a result of having an isolated
257 RBD domain. To identify preferential orientation of the RBD and specific amino acids involved in the
258 interaction with silica, three independent MD simulations were performed. The RBD was placed in a
259 simulation box, each simulation having a different orthogonal initial orientation with respect to the
260 surface of the nanoparticle (Supplementary Figure 2A-C). The silica surface was represented by a
261 planar slab of silica atoms, as the curvature of the SiO_2 NP is negligible for R_2/R_1=0.087. The positions
262 of the RBD with respect to the silica at the end point of each of the three simulations are shown in
263 Supplementary Figure 2D-F. In one out of the three simulations the RBD protein eventually lost contact

264 with the surface (Supplementary Figure 2F), possibly due to an unfavourable initial orientation. This
265 approach of probing several initial configurations identified the existence of the preferred protein-
266 material interface. The first simulation ended with the highest number of amino acids in close
267 proximity to the surface, possibly because the initial orientation allowed extensive contact within the
268 100 ns of the simulation (Figure 4A). A closer look at some of the residues involved, reveals that the
269 interaction is mediated by hydrogen bonds between the amino acids E340, R346 and K356, and the
270 hydroxyl groups of the silica (Figure 4B).

271 To better analyse the overall interaction of RBD with the silica, the minimum distances between each
272 residue and the silica surface were measured over the 100 ns for all three simulations (Supplementary
273 Figure 3). A subset of amino acids remained within a distance of 0.35 nm from the silica surface for a
274 cumulative time of 20 ns or longer. These 12 amino acids, which are the most likely residues involved
275 in the binding to silica, are highlighted in the RBD sequence in Supplementary Figure 4 and their
276 relevant distances to silica are summarised in Supplementary Table 1. To visualise the position of these
277 amino acids within the spike protein structure, the 12 residues are shown in yellow in Figure 5A. The
278 distribution of the points of contact suggests that the putative silica-binding motif of the RBD is well-
279 exposed on the external surface of the SARS-CoV-2 spike protein trimer. The analysis of the
280 electrochemical potential at the surface of the RBD reveals that the 12 residues involved in the binding
281 to silica are clustered together and form a patch of positive potential. This suggests that electrostatic
282 interactions of the positively charged patch with partially ionized hydroxyl groups may dominate the
283 overall interaction of the domain with silica, supplemented by the hydrogen bonds described above
284 (Figure 5B). The calculated isoelectric point of the RBD obtained from the biomolecular solvation and
285 electrostatics analyses was 8.78. The resulting mild overall average charge of approximately +2 at
286 pH=7.0 may also favour the adsorption of the RBD onto silica.

287 Interestingly, none of the amino acids that bind silica are known to be involved in the binding to ACE2,
288 which acts as the receptor of SARS-CoV-2 (pink spheres of Figure 5A). Consequently silica binding may

289 not prevent *per se* the interaction with ACE2, although the steric hindrance of the silica surface and
290 possible conformational changes due to adsorption will most likely affect binding to the receptor. To
291 establish whether silica-bound SARS-CoV-2 could still be able to bind ACE2 and subsequently infect
292 cells, an experimental confirmation would be essential.

293 Determination and analysis of the secondary structure of silica nanoparticle-adsorbed SARS-CoV-2
294 RBD

295 As the function of the RBD, besides its orientation, also depends on its structural integrity, RBD
296 structural changes following adsorption on SiO_2 NPs were investigated further using near-UV CD
297 analysis. To evaluate any changes in the protein secondary structure, CD spectra were collected from
298 RBD in solution and RBD adsorbed onto SiO_2 NPs. The spectra were corrected for the light scattering
299 caused by nanoparticles, whereas near-UV extinction spectra were used to correct for concentration
300 and normalise the CD spectra between samples (Supplementary Figure 5). Adsorption onto SiO_2 NPs
301 affected the overall CD spectrum, suggesting that bound RBD undergoes a conformational change
302 (Figure 6A). The nature and extent of the changes were further analysed by computing the secondary
303 structure estimation (SSE) of the CD spectra of Figure 6A using an established algorithm.[30] The
304 results of the analysis reveal a 25% increase of α-Helix and the proportional decrease of β-Strand
305 following interaction with SiO_2 NP (Figure 6).

306

307 In summary, a new geometrical model was developed and used to determine the maximum surface
308 occupancy of RBD proteins adsorbed on a spherical silica nanoparticle. The new model shows that
309 RBD occupies 32% of the maximum available space. The amino acids that are responsible for the RBD-
310 silica interaction were identified using MD simulations and mapped on the protein structure, showing
311 no overlap with the binding site of ACE2. Finally, silica binding triggers a conformational change that
312 is responsible for a 25% shift in the composition of RBD secondary structures.

313

314 4. Discussion

315 The new model requires only the relative mass M_r of the protein and assumes that a protein molecule
316 occupies a spherical volume, which limits the model to globular proteins. The radius R_2 of the sphere
317 that approximates the protein shape, determined using equation 3, does not require structural
318 information or experimental measurement, as would be the case for the gyration radius or the
319 hydrodynamic radius of a protein, and yet yields an accurate approximation of the protein size [12].
320 Equation 3 was used assuming an average partial specific volume $\bar{v}$ of 0.73 $cm^3\ g^{-1}$ for all the proteins
321 considered. However, $\bar{v}$ can be potentially corrected when evaluating proteins for which the value of
322 $\bar{v}$ is known to strongly differ from the average, for example in the case of highly glycosylated proteins
323 [33]. Overall, the good coefficient of determination obtained with the validation dataset (R^2=0.962)
324 suggests that the model is robust within a broad range of sizes and with a variety of proteins,
325 regardless of their exact shape and partial specific volume. For comparison, a previously reported
326 method to estimate the maximum number of molecules in the protein corona, calculated N_{max} by
327 estimating the surface area of the spherical nanoparticle, extended by the radius of the globular
328 protein, and dividing it by the cross-section of the protein [2]. However, when tested against the same
329 dataset as the one used in Figure 2B, the R^2 was 0.894, indicating a less accurate fit. Another previously
330 published geometrical model [34,35] was also tested against the same dataset and yielded a
331 coefficient of determination R^2=0.902. This model estimates the maximum surface occupancy
332 assuming that a 0.65 fraction of the volume of the spherical shell surrounding the nanoparticle is
333 effectively occupied by solid (F_{solid} = 0.65), whereas the remaining fraction (0.35) consists of the gaps
334 between the adsorbed proteins, also assumed spherical. The F_{solid} used was constant and independent
335 from the ratio R_2/R_1. The value F_{solid} = 0.65 was based on the earlier light scattering experiments on
336 microemulsions, for which the observed R_2/R_1 was very low and not entirely comparable with the case
337 of proteins adsorbed on nanoparticles [3]. Supplementary Figure 6, which is based on the new

338 geometrical model, demonstrates that within a more relevant range of R_2/R_1 as in Figure 2A, the
339 actual F_{solid} spans from 0.54 to 0.60, for R_2/R_1 of 0.6 and 0.1 respectively. That clearly indicates that at
340 the nanoscale sphere packing is not as efficient as in microemulsions. Our new model does take into
341 account that different R_2/R_1 values yield different packing densities and that explains the improved fit
342 when used with the experimental data as in Figure 2B. It might be possible to further improve the
343 model by using ellipsoids that better approximate the shape of each individual protein. However, this
344 would limit the use of the model to proteins with known structures whilst our model relies on the
345 protein mass only.

346 Our new geometrical model provides an analytical solution to the spheres-on-sphere packing problem
347 and if applied to the adsorption of proteins on nanoparticles, predicts theoretical maximum number
348 of molecules that can pack as a monolayer surrounding a spherical nanoparticle. A related but not
349 identical issue of adsorption kinetics of hard, non-interacting spherical particles or molecules on
350 planar surfaces has been studied in the past using Monte Carlo computer simulations. For example a
351 theoretical model describing kinetics and density of diffusion-driven irreversible adsorption assuming
352 a Random Sequential Adsorption (RSA) process, has been developed and used to calculate the number
353 of non-overlapping disks required to "block" a planar surface, where each disk represents a cross-
354 section of adsorbed particle [36]. RSA model predicts well the adsorption kinetics of colloids on planar
355 surfaces, such as mica and silica, and the theoretical findings have been validated using techniques
356 such as Atomic Force Microscopy (AFM) and Quartz Crystal Microbalance (QCM) [37,38].

357 The maximum jamming coverage Θ_{max} [37] is the ratio between the largest potential "blocked" surface
358 and the total area available and represents 2D equivalent of the maximum surface occupancy value
359 F_{solid} used in our model. For a planar surface and homogenous spheres, Θ_{max} converges to 0.547 [37],
360 which is far smaller than that of a hexagonal lattice of circles ($\pi\sqrt{3}/6 \approx 0.907$). This is expected because
361 the RSA model in [37] is based on the assumption of irreversible adsorption, where the disks, once
362 adsorbed, would not re-arrange their relative positions to maximise the packing. However, it has been

363 established experimentally that proteins adsorption on nanoparticles happens in three steps: (i) initial
364 reversible association, (ii) re-arrangement/re-orientation and (iii) irreversible binding or "hardening"
365 [39]. The ability of proteins to re-arrange their position once adsorbed on nanoparticles is likely to be
366 the reason why ours and earlier published data of nanoparticle-adsorbed proteins are consistent with
367 the model of hexagonal packing proposed here (Figure 2B). It is possible that extending RSA principle
368 by introducing a re-arrangement/re-orientation step in the Monte Carlo simulations studies and
369 complementing it by using our model for determining the maximum occupancy F_{solid}, would further
370 refine the problem of adsorption of proteins on spherical nanoparticles and could be beneficial for
371 fields such as nanomedicine. Whilst beyond the scope of this focussed study, such an extended
372 combined approach could be applied to study mixtures of proteins having a polydisperse size
373 distribution [40], like the case of nanoparticles exposed to blood plasma and subsequent formation of
374 a biomolecular corona that can affect the pharmacokinetics of nano-drugs and require complex
375 modelling to be fully understood and predicted [41,42].

376

377 The maximum amount of RBD bound to silica nanoparticles suggests a surface occupancy of 32% and
378 a K_D of 13.3 μg mL^{-1}. The sparse binding and moderately low affinity are likely due to electrostatic
379 repulsion between adjacent adsorbed RBD molecules, a phenomenon previously observed for
380 lysozyme adsorbed on silica nanoparticles at pH=7.0, for which a surface occupancy of 51% and K_D of
381 11 μg mL^{-1} were reported [43]. The isoelectric point of hen egg lysozyme estimated from its amino
382 acid sequence is 9.3 which makes lysozyme positively charged at neutral pH [44]. The surface
383 occupancy and affinity of lysozyme for silica drops to 31% and 50 μg mL^{-1} at pH=6.1, as a consequence
384 of stronger electrostatic repulsion, but increases to 86% and 1.4 μg mL^{-1} at higher pH=8.3, at which
385 the protein overall charge is nearly neutral [43]. Although the binding of RBD to the silica surface at
386 physiological pH appears to be sparse, the moderate surface occupancy of RBD is unlikely to be a
387 limiting factor for the adhesion of viral particles onto silica surfaces. In fact the average distance

388 between the RBD molecules bound to silica, depicted in the inset of Figure 3, is identical to that
389 between the three RBDs within individual trimeric S proteins (PDB ID: 6VXX) and is far smaller than
390 the distance between adjacent spike proteins on the same viral particle, which is about 20 nm [32].
391 Therefore, even the detected 32% occupancy would be sufficient to engage all RBDs on all adjacent S
392 proteins exposed on the surface of a typical virus. Also, the presence of several spike proteins on each
393 viral particle is likely to further promote binding via an avidity effect, which may compensate the
394 relatively low affinity measured for individual RBD-silica interaction. The uncertainty fitting the affinity
395 constant was large, due to the need to experimentally measure a broad range of unbound RBD protein
396 concentrations. Accurate values of K_D for proteins adsorbed on SiO_2 nanoparticles were previously
397 obtained for Human Serum Albumin (2.8 μM), Transferrin (650 nM), Glutathione S-Transferase (54
398 nM), Fibrinogen (11 nM), Plasma Coagulation Factor XII (8 nM) using microscale thermophoresis,
399 differential centrifugal sedimentation or dynamic light scattering [45–47]. Our method is likely to be
400 useful and informative when studying binding properties of individual proteins with respect to a panel
401 of different materials available in the form of nanoparticles. Although the binding properties of the
402 assembled virus may not be reliably estimated based on the K_D measured for individual protein
403 domains, such information may help to dissect the mechanisms of viral adhesion on different
404 materials.

405

406 MD simulations were focused on RBD binding to silica and have indicated that the silica interacts with
407 the external solvent-exposed part of the RBD and thus confirmed that such interaction is genuine and
408 is unlikely to be affected by the core of the RBD exposed by the truncation of the spike protein. MD
409 simulations of the full-length spike protein were beyond the scope of this work, as the computational
410 work described here was primarily intended to support the experimental RBD binding data. MD
411 simulations of the interaction between the full spike complex and solid materials such as graphite and
412 cellulose have been performed recently [10]. That recent study revealed that the RBD is the main area

413 of contact between the spike complex and hydrophilic cellulose (75% of all contacts are within the
414 RBD). On the other hand, in the case of the hydrophobic graphite, after an initial phase of adsorption
415 that also involves the RBD, the protein structure shows some deformations and more extensive
416 contacts after 100 ns, suggesting that hydrophobic materials may affect protein tertiary structure
417 more than hydrophilic surfaces. Neither that nor our study detected any substantial changes of the
418 secondary structure during the simulations (100 ns in both cases). The structural rearrangement of
419 proteins at the solid-liquid interface, also referred to as "hardening" [39,47], is likely beyond the time
420 scale of MD simulations. The slight change of secondary structure observed using CD spectroscopy
421 could not be confirmed by the simulations, which were primarily intended to study the likely
422 orientation and contacts of the RBD on a silica surface. Importantly, MD confirmed the amino acids
423 identified in Figure 5 (yellow spheres) as genuine candidates for a putative silica-binding sub-domain
424 within the RBD. Such sub-domain could potentially be engineered into silica-binding peptide aptamers,
425 useful for the decoration of functionalised glass-chips or similar applications [48]. Interestingly, the
426 amino acids found in contact with silica were different to those binding cellulose. Although only a
427 partial information was made available by the authors, the findings suggest that the RBD-surface
428 interaction is material specific [10].

429

430 The study of structural changes was limited to the secondary structure, as this was considered suitable
431 to provide an accessible assessment of the effect that adsorption on silica has on the structure of RBD.
432 CD spectroscopy provides routine and reliable structural data from proteins in solution. In this work
433 we further improved the use of CD for the study of protein adsorbed on colloidal suspensions by
434 introducing a correction of the scattering due to nanoparticles using near-UV extinction spectra.
435 Although some CD spectra were acquired using the top-end Synchrotron Radiation CD instrument
436 available at Diamond Light Source, the spectra from colloidal suspensions were also obtained using a
437 benchtop instrument, to illustrate the accessibility of the overall method.

438 The increase of α-Helix content and the proportional reduction of β-Strand observed upon adsorption
439 on silica nanoparticles was unexpected. In the past opposite conformational changes have been
440 reported more often. For example, the α-Helix content of albumin from bovine serum decreased in a
441 pH-dependent manner when exposed to 15 nm silica nanoparticles [49] and that of lysozyme also
442 decreased following adsorption on a glass surface [50]. However, the RBD domain of the SARS-CoV-2
443 spike protein seems to be prone to a shift of secondary structures in the opposite direction, as
444 evidenced by a 7% increment of α-Helix content and associated decrease by 7% of β-Strand following
445 binding to the ACE2 receptor, based on PDB structures 6M17 (ACE2-bound) and 6VXX (unbound)
446 [13,51]. That well documented naturally occurring protein-protein interaction indicates that such an
447 increase in helical content of RBD is possible in principle. The extent of RBD-silica binding interface
448 (Figure 5B) may be the reason for the even larger shift towards α-Helix, observed upon binding of RBD
449 to silica nanoparticles.

450

451 Silica is a highly abundant solid material that mimics well ordinary glass surfaces such as mobile phone
452 screens, drinking utensils, medical equipment and is used widely in water filtration, construction,
453 paints and coatings. The abundance of silica transforms such materials into copious reservoirs where
454 the virus can potentially accumulate and therefore requires specific attention. Data published so far
455 focused on the infectivity of viral particles exposed to different surfaces, including silica, as adsorption
456 on solid materials appears to be relevant to potential surface transmission of the virus. Our study
457 complements these by deciphering the molecular mechanisms involved in the binding of viral proteins
458 to solid surfaces.

459 Future experiments using nanoparticles made of materials other than silica could be used to study the
460 potential impact of specific materials on the surface-virus interaction and on the spreading of virus
461 particles, based on the extent of observed retention and denaturation of the viral proteins. Whereas
462 materials or engineered surfaces characterised by limited retention (low affinity and sparse packing)

463 would only pose limited risk of surface transmission, materials with high retention and limited
464 denaturation would be likely able to accumulate infective particles and promote transmission.
465 Materials or engineered surfaces that can accumulate viral particles efficiently, due to good binding
466 properties, but at the same time they would have the ability to denature and perhaps inactivate the
467 viral proteins have the potential to be used as active antiviral surfaces [52,53], active components
468 within personal protective equipment [54] and, when in the form of nanoparticles, could present
469 nano-antiviral properties typical of so-called hard nanomaterials [55]. Importantly, in the context of
470 the discovery of new hard nanomaterials, the concepts developed in this work would be particularly
471 useful, as the methodology is nanoparticle-focused and therefore allows the use of in-solution
472 methods to study protein-solid materials interactions.

473

474 5. Conclusions

475 A new model to describe protein packing on spherical particles was developed and validated using an
476 existing dataset of nanoparticle-bound globular proteins [31]. The new model proposes that proteins
477 adsorbed at maximum density assemble in a quasi-hexagonal pattern projected onto the spherical
478 surface of the nanoparticle. The proposed model fits experimental data better than previously
479 published packing models [2,3,34,35]. The new model has been applied to quantitatively describe the
480 fraction of the spherical shell of 50 nm silica nanoparticles occupied by proteins upon exposure to the
481 SARS-CoV-2 receptor binding domain (RBD) at physiological pH. The experimental model used in this
482 study was created to study the ability of silica glass materials to interact with viral particles. The
483 binding of viral surface proteins was found to be sparse compared to the highest theoretically
484 achievable density (32% of the maximum packing). This observation is consistent with previously
485 reported binding densities to silica nanoparticles of other proteins, such as hen egg lysozyme [43]. The
486 likely RBD-silica binding interface was identified using molecular dynamics simulations and the
487 residues involved appear to be material-specific, as they are different from those involved in the

488 binding of RBD to graphite and cellulose that were previously identified [10]. The change of RBD's
489 secondary structure upon adsorption on silica nanoparticles was determined using circular dichroism
490 spectroscopy, to assess whether silica-adsorbed RBD preserves its overall structure. A 25% shift from
491 β-Strand to α-Helix was found, which suggests substantial conformational changes upon adsorption
492 at the solid liquid interface. Overall, the study provides new insights into the extent of binding, likely
493 orientation and loss of structural integrity of the RBD upon binding to silica nanoparticles. These
494 results were obtained using an integrated and accessible approach, combining experimental and
495 computational methods, which can be used as a blueprint for future studies of different surfaces. The
496 mechanistic understanding of the adsorption of viral particles onto solid surfaces can ultimately
497 contribute to containing the spread of SARS-CoV-2 or other viruses.

498

499 Declaration of Competing Interest

500 There are no conflicts to declare.

501

502 Acknowledgements

503 We thank Diamond Light Source for experimental beamtime on B23 allocated within the SM27024
504 Rapid Access proposal. This work used the Isambard UK National Tier-2 HPC Service
505 (http://gw4.ac.uk/isambard/) operated by GW4 and the UK Met Office and funded by EPSRC
506 (EP/P020224/1).

References

[1] M. Rabe, D. Verdes, S. Seeger, Understanding protein adsorption phenomena at solid surfaces, Adv. Colloid Interface Sci. 162 (2011) 87–106.

https://doi.org/http://dx.doi.org/10.1016/j.cis.2010.12.007.

[2] D. Dell'Orco, M. Lundqvist, C. Oslakovic, T. Cedervall, S. Linse, Modeling the time evolution of the nanoparticle-protein corona in a body fluid., PLoS One. 5 (2010) e10949. https://doi.org/10.1371/journal.pone.0010949.

[3] D.J. Cebula, R.H. Ottewill, J. Ralston, P.N. Pusey, Investigations of microemulsions by light scattering and neutron scattering, J. Chem. Soc. Faraday Trans. 1 Phys. Chem. Condens. Phases. 77 (1981) 2585. https://doi.org/10.1039/f19817702585.

[4] A.A. Shemetov, I. Nabiev, A. Sukhanova, Molecular Interaction of Proteins and Peptides with Nanoparticles, ACS Nano. 6 (2012) 4585–4602. https://doi.org/10.1021/nn300415x.

[5] N. Van Doremalen, T. Bushmaker, D.H. Morris, M.G. Holbrook, A. Gamble, B.N. Williamson, A. Tamin, J.L. Harcourt, N.J. Thornburg, S.I. Gerber, J.O. Lloyd-Smith, E. De Wit, V.J. Munster, Aerosol and surface stability of SARS-CoV-2 as compared with SARS-CoV-1, N. Engl. J. Med. 382 (2020) 1564–1567. https://doi.org/10.1056/NEJMc2004973.

[6] F. Carraturo, C. Del Giudice, M. Morelli, V. Cerullo, G. Libralato, E. Galdiero, M. Guida, Persistence of SARS-CoV-2 in the environment and COVID-19 transmission risk from environmental matrices and surfaces, Environ. Pollut. 265 (2020) 115010. https://doi.org/10.1016/j.envpol.2020.115010.

[7] G. Kampf, D. Todt, S. Pfaender, E. Steinmann, Persistence of coronaviruses on inanimate surfaces and their inactivation with biocidal agents, J. Hosp. Infect. 104 (2020) 246–251. https://doi.org/10.1016/j.jhin.2020.01.022.

[8] S. Ratnesar-Shumate, G. Williams, B. Green, M. Krause, B. Holland, S. Wood, J. Bohannon, J. Boydston, D. Freeburger, I. Hooper, K. Beck, J. Yeager, L.A. Altamura, J. Biryukov, J. Yolitz, M. Schuit, V. Wahl, M. Hevey, P. Dabisch, Simulated Sunlight Rapidly Inactivates SARS-CoV-2 on Surfaces, J. Infect. Dis. 222 (2020) 214–222. https://doi.org/10.1093/infdis/jiaa274.

[9] S. Riddell, S. Goldie, A. Hill, D. Eagles, T.W. Drew, The effect of temperature on persistence of SARS-CoV-2 on common surfaces, Virol. J. 17 (2020) 145. https://doi.org/10.1186/s12985-020-01418-7.

[10] D.C. Malaspina, J. Faraudo, Computer simulations of the interaction between SARS-CoV-2 spike glycoprotein and different surfaces, Biointerphases. 15 (2020) 051008. https://doi.org/10.1116/6.0000502.

[11] E.B. Saff, A.B.J. Kuijlaars, Distributing many points on a sphere, Math. Intell. 19 (1997) 5–11. https://doi.org/10.1007/BF03024331.

[12] H.P. Erickson, Size and Shape of Protein Molecules at the Nanometer Level Determined by Sedimentation, Gel Filtration, and Electron Microscopy, Biol. Proced. Online. 11 (2009) 32–51. https://doi.org/10.1007/s12575-009-9008-x.

[13] R. Yan, Y. Zhang, Y. Li, L. Xia, Y. Guo, Q. Zhou, Structural basis for the recognition of SARS-CoV-2 by full-length human ACE2, Science (80-.). 367 (2020) 1444–1448. https://doi.org/10.1126/science.abb2762.

[14] S. Jo, T. Kim, V.G. Iyer, W. Im, CHARMM-GUI: A web-based graphical user interface for CHARMM, J. Comput. Chem. 29 (2008) 1859–1865. https://doi.org/10.1002/jcc.20945.

[15] J. Lee, X. Cheng, J.M. Swails, M.S. Yeom, P.K. Eastman, J.A. Lemkul, S. Wei, J. Buckner, J.C. Jeong, Y. Qi, S. Jo, V.S. Pande, D.A. Case, C.L. Brooks, A.D. MacKerell, J.B. Klauda, W. Im, CHARMM-GUI Input Generator for NAMD, GROMACS, AMBER, OpenMM, and CHARMM/OpenMM Simulations Using the CHARMM36 Additive Force Field, J. Chem. Theory Comput. 12 (2016) 405–413. https://doi.org/10.1021/acs.jctc.5b00935.

[16] F.S. Emami, V. Puddu, R.J. Berry, V. Varshney, S. V. Patwardhan, C.C. Perry, H. Heinz, Prediction of specific biomolecule adsorption on silica surfaces as a function of pH and particle size, Chem. Mater. 26 (2014) 5725–5734. https://doi.org/10.1021/cm5026987.

[17] W.L. Jorgensen, J. Chandrasekhar, J.D. Madura, R.W. Impey, M.L. Klein, Comparison of simple potential functions for simulating liquid water, J. Chem. Phys. 79 (1983) 926–935. https://doi.org/10.1063/1.445869.

[18] B.R. Brooks, C.L. Brooks, A.D. Mackerell, L. Nilsson, R.J. Petrella, B. Roux, Y. Won, G. Archontis, C. Bartels, S. Boresch, A. Caflisch, L. Caves, Q. Cui, A.R. Dinner, M. Feig, S. Fischer, J. Gao, M. Hodoscek, W. Im, K. Kuczera, T. Lazaridis, J. Ma, V. Ovchinnikov, E. Paci, R.W. Pastor, C.B. Post, J.Z. Pu, M. Schaefer, B. Tidor, R.M. Venable, H.L. Woodcock, X. Wu, W. Yang, D.M. York, M. Karplus, CHARMM: The biomolecular simulation program, J. Comput. Chem. 30 (2009) 1545–1614. https://doi.org/10.1002/jcc.21287.

[19] W.G. Hoover, Canonical dynamics: Equilibrium phase-space distributions, Phys. Rev. A. 31 (1985) 1695–1697. https://doi.org/10.1103/PhysRevA.31.1695.

[20] M. Parrinello, A. Rahman, Polymorphic transitions in single crystals: A new molecular dynamics method, J. Appl. Phys. 52 (1981) 7182–7190. https://doi.org/10.1063/1.328693.

[21] S. Nosé, M.L. Klein, Constant pressure molecular dynamics for molecular systems, Mol. Phys. 50 (1983) 1055–1076. https://doi.org/10.1080/00268978300102851.

[22] B. Hess, H. Bekker, H.J.C. Berendsen, J.G.E.M. Fraaije, LINCS: A linear constraint solver for molecular simulations, J. Comput. Chem. 18 (1997) 1463–1472. https://doi.org/10.1002/(SICI)1096-987X(199709)18:12<1463::AID-JCC4>3.0.CO;2-H.

[23] S. Miyamoto, P. Kollman, Settle: An analytical version of the SHAKE and RATTLE algorithm for rigid water models, J. Comput. Chem. 13 (1992) 952–962. citeulike-article-id:1172605 http://dx.doi.org/10.1002/jcc.540130805.

[24] T. Darden, D. York, L. Pedersen, Particle mesh Ewald: An N ·log(N) method for Ewald sums in large systems, J. Chem. Phys. 98 (1993) 10089–10092. https://doi.org/10.1063/1.464397.

[25] N.A. Baker, D. Sept, S. Joseph, M.J. Holst, J.A. McCammon, Electrostatics of nanosystems:

application to microtubules and the ribosome., Proc. Natl. Acad. Sci. U. S. A. 98 (2001) 10037–41. https://doi.org/10.1073/pnas.181342398.

[26] APBS-PDB2PQR software suite, (2021). https://server.poissonboltzmann.org (accessed June 17, 2021).

[27] T.J. Dolinsky, J.E. Nielsen, J.A. McCammon, N.A. Baker, PDB2PQR: An automated pipeline for the setup of Poisson-Boltzmann electrostatics calculations, Nucleic Acids Res. 32 (2004) W665–W667. https://doi.org/10.1093/nar/gkh381.

[28] E.F. Pettersen, T.D. Goddard, C.C. Huang, G.S. Couch, D.M. Greenblatt, E.C. Meng, T.E. Ferrin, UCSF Chimera--a visualization system for exploratory research and analysis., J. Comput. Chem. 25 (2004) 1605–12. https://doi.org/10.1002/jcc.20084.

[29] R. Hussain, K. Benning, D. Myatt, T. Javorfi, E. Longo, T.R. Rudd, B. Pulford, G. Siligardi, CDApps : integrated software for experimental planning and data processing at beamline B23, Diamond Light Source. Corrigendum, J. Synchrotron Radiat. 22 (2015) 862–862. https://doi.org/10.1107/S1600577515007602.

[30] S.W. Provencher, J. Glöckner, Estimation of Globular Protein Secondary Structure from Circular Dichroism, Biochemistry. 20 (1981) 33–37. https://doi.org/10.1021/bi00504a006.

[31] C. De Roe, P.J. Courtoy, P. Baudhuin, A model of protein-colloidal gold interactions., J. Histochem. Cytochem. 35 (1987) 1191–1198. https://doi.org/10.1177/35.11.3655323.

[32] H. Yao, Y. Song, Y. Chen, N. Wu, J. Xu, C. Sun, J. Zhang, T. Weng, Z. Zhang, Z. Wu, L. Cheng, D. Shi, X. Lu, J. Lei, M. Crispin, Y. Shi, L. Li, S. Li, Molecular Architecture of the SARS-CoV-2 Virus, Cell. 183 (2020) 1–9. https://doi.org/10.1016/j.cell.2020.09.018.

[33] H. Durchschlag, Determination of the partial specific volume of conjugated proteins, Colloid Polym. Sci. 267 (1989) 1139–1150. https://doi.org/10.1007/BF01496937.

[34] L. Calzolai, F. Franchini, D. Gilliland, F. Rossi, Protein–Nanoparticle Interaction: Identification of the Ubiquitin–Gold Nanoparticle Interaction Site, Nano Lett. 10 (2010) 3101–3105. https://doi.org/10.1021/nl101746v.

[35] H. Mattoussi, J.M. Mauro, E.R. Goldman, G.P. Anderson, V.C. Sundar, F. V. Mikulec, M.G. Bawendi, Self-Assembly of CdSe–ZnS Quantum Dot Bioconjugates Using an Engineered Recombinant Protein, J. Am. Chem. Soc. 122 (2000) 12142–12150. https://doi.org/10.1021/ja002535y.

[36] Z. Adamczyk, Kinetics of diffusion-controlled adsorption of colloid particles and proteins, J. Colloid Interface Sci. 229 (2000) 477–489. https://doi.org/10.1006/jcis.2000.6993.

[37] M. Nattich-Rak, A. Pomorska, P. Batys, Z. Adamczyk, Adsorption kinetic of myoglobin on mica and silica – Role of electrostatic interactions, Colloids Surfaces B Biointerfaces. 198 (2021) 111436. https://doi.org/10.1016/j.colsurfb.2020.111436.

[38] C.A. Johnson, A.M. Lenhoff, Adsorption of charged latex particles on mica studied by atomic force microscopy, J. Colloid Interface Sci. 179 (1996) 587–599. https://doi.org/10.1006/jcis.1996.0253.

[39] A. Wang, K. Vangala, T. Vo, D. Zhang, N.C. Fitzkee, A Three-Step Model for Protein–Gold Nanoparticle Adsorption, J. Phys. Chem. C. 118 (2014) 8134–8142. https://doi.org/10.1021/jp411543y.

[40] Z. Adamczyk, B. Siwek, M. Zembala, P. Weroński, Influence of polydispersity on random sequential adsorption of spherical particles, J. Colloid Interface Sci. 185 (1997) 236–244. https://doi.org/10.1006/jcis.1996.4540.

[41] D. Docter, D. Westmeier, M. Markiewicz, S. Stolte, S.K. Knauer, R.H. Stauber, The nanoparticle biomolecule corona: lessons learned - challenge accepted?, Chem. Soc. Rev. 44 (2015) 6094–6121. https://doi.org/10.1039/c5cs00217f.

[42] P. Dogra, J.D. Butner, Y. li Chuang, S. Caserta, S. Goel, C.J. Brinker, V. Cristini, Z. Wang, Mathematical modeling in cancer nanomedicine: a review, Biomed. Microdevices. 21 (2019) 1–23. https://doi.org/10.1007/s10544-019-0380-2.

[43] B. Bharti, J. Meissner, G.H. Findenegg, Aggregation of silica nanoparticles directed by adsorption of lysozyme, Langmuir. 27 (2011) 9823–9833. https://doi.org/10.1021/la201898v.

[44] M.R. Wilkins, E. Gasteiger, A. Bairoch, J.C. Sanchez, K.L. Williams, R.D. Appel, D.F. Hochstrasser, Protein identification and analysis tools in the ExPASy server., Methods Mol. Biol. 112 (1999) 531–552. https://doi.org/10.1385/1-59259-584-7:531.

[45] O. Vilanova, J.J. Mittag, P.M. Kelly, S. Milani, K.A. Dawson, J.O. Rädler, G. Franzese, Understanding the Kinetics of Protein–Nanoparticle Corona Formation, ACS Nano. 10 (2016) 10842–10850. https://doi.org/10.1021/acsnano.6b04858.

[46] F. Hao, Q.S. Liu, X. Chen, X. Zhao, Q. Zhou, C. Liao, G. Jiang, Exploring the Heterogeneity of Nanoparticles in Their Interactions with Plasma Coagulation Factor XII, ACS Nano. (2019). https://doi.org/10.1021/acsnano.8b08471.

[47] W. Ma, A. Saccardo, D. Roccatano, D. Aboagye-Mensah, M. Alkaseem, M. Jewkes, F. Di Nezza, M. Baron, M. Soloviev, E. Ferrari, Modular assembly of proteins on nanoparticles, Nat. Commun. 9 (2018) 1489. https://doi.org/10.1038/s41467-018-03931-4.

[48] M.-E. Aubin-Tam, D.C. Appleyard, E. Ferrari, V. Garbin, O.O. Fadiran, J. Kunkel, M.J. Lang, Adhesion through Single Peptide Aptamers, J. Phys. Chem. A. 115 (2011) 3657–3664. https://doi.org/10.1021/jp1031493.

[49] A. Kondo, S. Oku, K. Higashitani, Structural changes in protein molecules adsorbed on ultrafine silica particles, J. Colloid Interface Sci. 143 (1991) 214–221. https://doi.org/https://doi.org/10.1016/0021-9797(91)90454-G.

[50] A.A. Thyparambil, Y. Wei, R.A. Latour, Experimental characterization of adsorbed protein

orientation, conformation, and bioactivity, Biointerphases. 10 (2015) 019002. https://doi.org/10.1116/1.4906485.

[51] A.C. Walls, Y.J. Park, M.A. Tortorici, A. Wall, A.T. McGuire, D. Veesler, Structure, Function, and Antigenicity of the SARS-CoV-2 Spike Glycoprotein, Cell. 181 (2020) 281-292.e6. https://doi.org/10.1016/j.cell.2020.02.058.

[52] Z. Sun, K. (Ken) Ostrikov, Future antiviral surfaces: Lessons from COVID-19 pandemic, Sustain. Mater. Technol. 25 (2020) e00203. https://doi.org/10.1016/j.susmat.2020.e00203.

[53] M.C. Sportelli, M. Izzi, E.A. Kukushkina, S.I. Hossain, R.A. Picca, N. Ditaranto, N. Cioffi, Can Nanotechnology and Materials Science Help the Fight against SARS-CoV-2?, Nanomaterials. 10 (2020) 802. https://doi.org/10.3390/nano10040802.

[54] L.M. Pandey, Surface engineering of personal protective equipments (PPEs) to prevent the contagious infections of SARS-CoV-2, Surf. Eng. 36 (2020) 901–907. https://doi.org/10.1080/02670844.2020.1801034.

[55] G. Reina, S. Peng, L. Jacquemin, A.F. Andrade, A. Bianco, Hard Nanomaterials in Time of Viral Pandemics, ACS Nano. 14 (2020) 9364–9388. https://doi.org/10.1021/acsnano.0c04117.

Figures

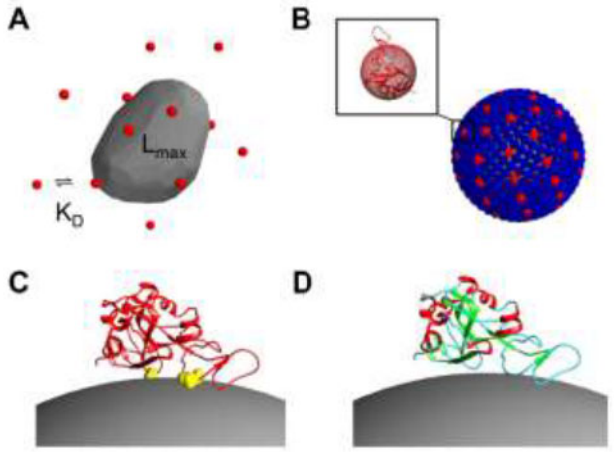

Figure 1. Schematic of the main aspects investigated in this study. (A) Determination of the binding properties of RBD onto solid nanoparticles. (B) Development of a geometrical model to define the number of bound protein (red spheres) compared to the maximum theoretical surface occupancy (blue spheres). (C) Determination of the preferential orientation of RBD on silica nanoparticles and identification of the amino acids involved in the binding (yellow spheres). (D) Assessment of RBD secondary structure changes upon adsorption on silica nanoparticles (red = α-Helix, green = β-strand, cyan = unordered).

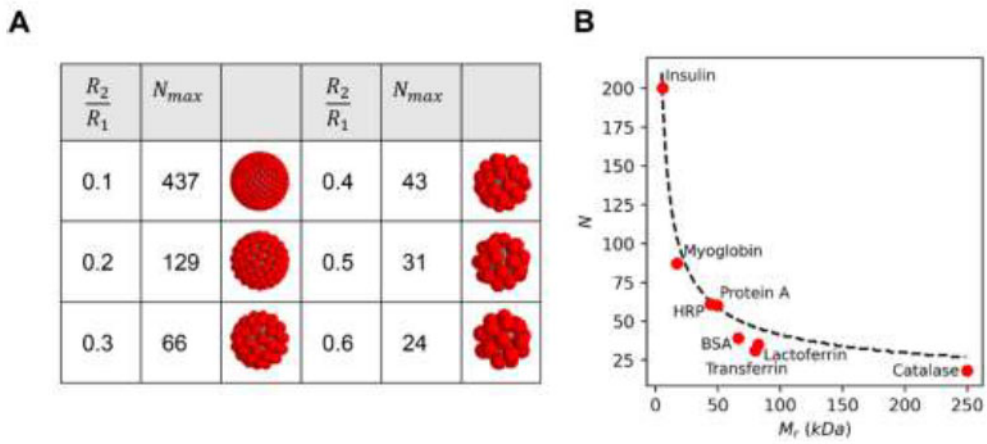

Figure 2. Geometrical model of the maximum surface occupancy of globular proteins on spherical nanoparticles. (A) Examples of the maximum number of proteins per particle (N_{max}) and their visualisation for representative values of the ratio between the protein radius (R_2) and the particle radius (R_1). (B) Validation of the new geometrical model (dashed line) with measured values of N_{max} for several globular proteins (red circles) [27]. The coefficient of determination R^2 is 0.962.

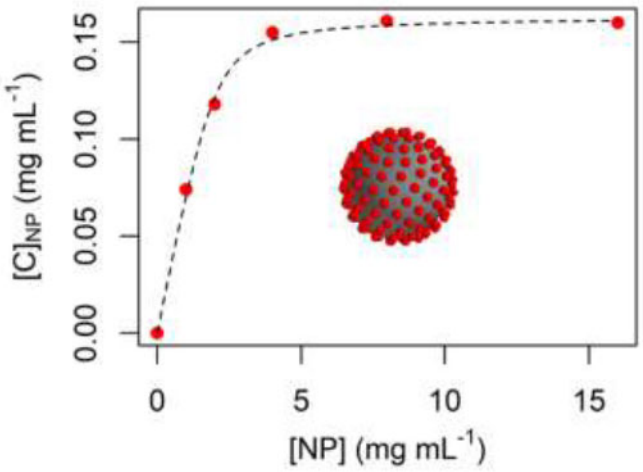

Figure 3. RBD adsorption onto silica nanoparticles. The experimental values (red points) of bound protein $[C]_{NP}$ versus nanoparticle concentration [NP] are fitted with the Hill-Langmuir equation to calculate the binding parameters L_{max} and K_D. The grey sphere in the figure represents a 50 nm silica nanoparticle surrounded by RBD molecules (red spheres) to visualise the measured 32% surface occupancy (figure to scale).

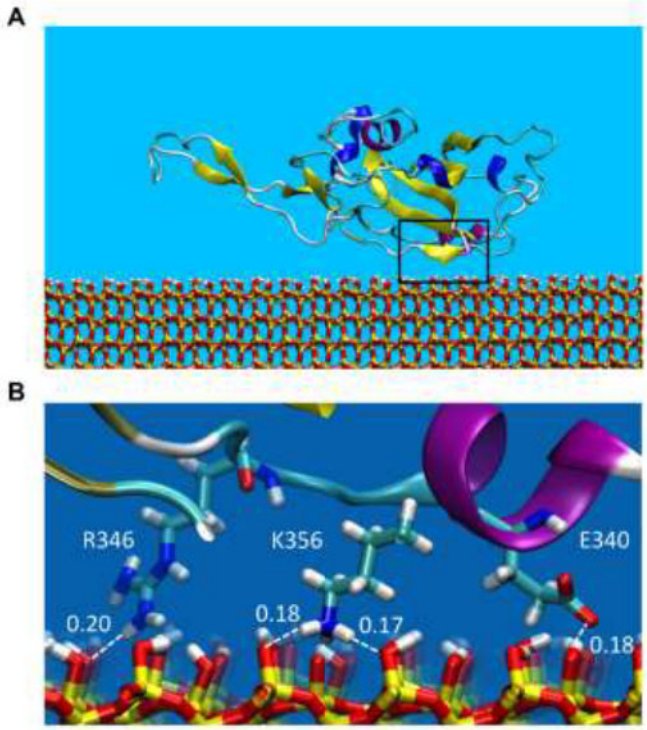

Figure 4. MD simulations of RBD-silica interaction. (A) Representation of the RBD adsorbed on silica in a representative configuration at the end point of simulation 1. The rectangle highlights the area of contact detailed in panel B. (B) Detailed representation of three residues in close contact with silica: arginine 346 (R346), lysine 356 (K356) and glutamic acid 340 (E340) from left to right. The distances between hydrogen and oxygen atoms at the interface are indicated and are compatible with the hydrogen bonds length.

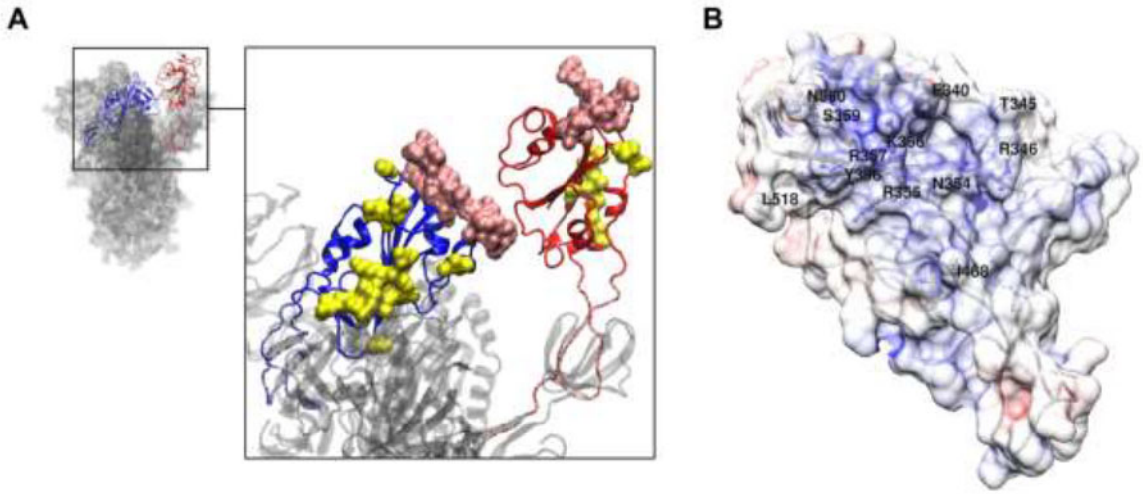

Figure 5. The silica-binding site of the RBD. (A) Two of the three RBDs of the spike complex of SARS-CoV-2 (grey ribbons) are highlighted in blue and red to allow visualisation of the area of interest from multiple angles. The amino acids represented as yellow spheres in the inset are those which were found in contact with the silica surface for longer than 20 ns in each of three distinct MD simulations. The amino acids highlighted in pink are those involved in the binding to the ACE2 receptor. (B) Calculated electrochemical potential at the surface of the RBD. Red shades represent negative potential, blue indicates positive potential. The labels identify the residues in contact with the silica (depicted in yellow in panel A), which occupy a large positive patch on the surface of the RBD.

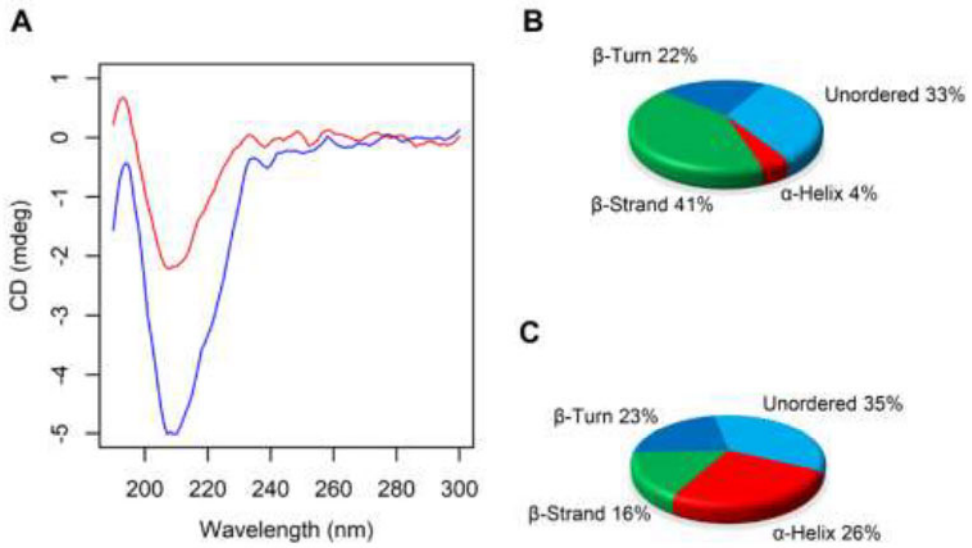

Figure 6. RBD secondary structure change upon adsorption onto silica nanoparticles. (A) CD spectra of RBD in solution (red) and silica-bound RBD (blue). The secondary structure estimation obtained from the spectra is represented as pie charts for both the RBD in solution (B) and bound RBD (C), showing a 25% shift in secondary structures upon adsorption on silica, primarily an increment of α-helices at the expenses of β-strands.

Modelling the adsorption of proteins to nanoparticles at the solid-liquid interface – Supplementary information

Mikhail Soloviev,[a] Giuliano Siligardi,[b] Danilo Roccatano[c] and Enrico Ferrari[†d]

[a] Department of Biological Sciences, Royal Holloway University of London, Egham TW20 0EX, UK.
[b] Diamond Light Source, Diamond House, Chilton, Didcot OX11 0DE, UK.
[c] School of Mathematics and Physics, University of Lincoln, Lincoln LN6 7TS, UK.
[d] School of Life Sciences, University of Lincoln, Lincoln LN6 7TS, UK.
[†] Address correspondence to eferrari@lincoln.ac.uk

1. Supplementary Methods

1.1. Geometrical model

The problem of minimizing the distance between N points on a sphere is generally referred to as the Tammes's problem, from the name of the botanist who studied the distribution of pores on pollen grains. For some given N, spherical tiling can be obtained by placing the N points in the centre of regular hexagons and pentagons forming regular spherical polyhedra. The football is the most well-known example of such solids. In polyhedral combinatorics, the topological invariant known as Euler-Poincaré characteristic of any spherical polyhedron is always 2. This means that the sum of the number of vertices and faces forming the solid, minus the number of edges is always 2. For the case of solid spherical polyhedra made of hexagons and pentagons and having three polygons meeting at each vertex, Leonhard Euler demonstrated that the condition is met whenever the number of pentagons is 12, whereas the number of hexagons is unconstrained. For a large N, the number of hexagons overwhelms the pentagons, so that the asymptotic result of the Tammes's problem can be simplified by projecting a planar hexagonal tiling onto a sphere. This minimises the distance between adjacent spheres packed on another sphere in the same way as hexagonal tiling maximises the packing of spheres on a planar surface.

The relationship between N and the minimum angular distance δ_N between two points at the centre of two adjacent hexagons projected onto a sphere can be obtained by equating the area of the unit sphere to the total area of a hexagonal lattice with N points at the centre of each cell, each having an area of $\sqrt{3}/2$. The scaling factor δ_N^2 can be obtained by equating total areas as shown in supplementary equation 1.

$$N\frac{\sqrt{3}}{2}\delta_N^2 = 4\pi \qquad \text{(supplementary equation 1)}$$

By rearranging supplementary equation 1 for N and by calculating the floor of the resulting N, the approximation of the maximum number of equidistant points that fit on a sphere can be found, as shown by supplementary equation 2.

$$N = \left\lfloor \frac{8\sqrt{3}}{3}\pi\frac{1}{\delta_N^2} \right\rfloor \qquad \text{(supplementary equation 2)}$$

When N points are replaced by N spheres of radius R_2 surrounding a sphere of radius R_1, the condition that minimizes the angular distance is $\delta_N = 2\alpha$, with α being the angle between the segments AB and AC depicted in supplementary figure 1, and B and D being two adjacent points of the N points at the centre of the packed spheres. Equation 1 in the Experimental section has been obtained by replacing

$\delta_N = 2\alpha$ in supplementary equation 2, whereas equation 2 was obtained using simple geometrical considerations based on the squared triangle ABC depicted in supplementary figure 1.

Limits of validity of the new geometrical model

To define the limit of validity of the model, the ratio between the surface area of the sphere of radius R_1+R_2 (A_{sphere}) and the total area of N hexagons circumscribed to the spheres of radius R_2 surrounding the previous sphere ($N \cdot A_{hexagon}$) was calculated. The hexagons were placed in such a way that the centre of each polygon would be on a segment like AB in supplementary figure 1 and the common side of an adjacent hexagon would include the point C. In these conditions, the inradius of the hexagon would be equal to $\frac{R_2}{\cos\alpha}$. Using N calculated according to the new module, the resulting ratio between the total area of the sphere and the area of the projected hexagonal tiling is described by supplementary equation 3.

$$\frac{A_{sphere}}{N \times A_{hexagon}} = \frac{(R_1+R_2)^2}{R_2^2} \times (\cos\alpha)^2 \times \frac{4\pi}{2\sqrt{3}N} = \left(\frac{\alpha}{\tan\alpha}\right)^2 \qquad \text{(supplementary equation 3)}$$

Values of this ratio approaching 1 are expected for large N, where the number of pentagons in ideal solid spherical polyhedra is negligible compared to the hexagons, so that hexagon-only polyhedra would approximate sufficiently well the total area of the sphere. On the contrary, for small N, the projection of a planar hexagon tiling onto a sphere tends to overestimate the available surface area, as in a regular polyhedron 12 tiles have to be pentagons, which have a smaller area than hexagons circumscribed in circles of the same size. For example, for the extreme case R_2/R_1=1 (spheres surrounding a sphere of the same size), the resulting N is 13. However, the actual number of non-overlapping spheres that can surround a sphere of the same size, defined as the kissing number in the 3 dimensions, is known to be 12. This highlights that the model described has limitations for large values of R_2/R_1, for which a spherical tiling made of hexagons only is not a good approximation of the actual spherical area, and the resulting geometry with N surrounding spheres would be characterised by substantial overlaps.

Solutions of supplementary equation 3 were numerical calculated for a broad range of R_2/R_1 and values of the surface area ratio larger than 0.9 were found for R_2/R_1<0.61. This means that, in this range, the surface area approximated by projected hexagons gives acceptable values within 10% of the actual spherical surface. Based on this calculation, $R_2/R_1 \leq 0.6$ was used as a reasonable limit of validity of this model, where minor overlaps between surrounding spherical proteins would be likely compensated by conformational changes or simply by the fact that actual proteins are not exactly spherical.

Comparison of the new model with a previously reported geometrical approach

As described in the discussion, the literature reports works where the maximum number N_{max} of spherical proteins surrounding a nanoparticle was determined using supplementary equation 4, based on a simple geometrical model originally developed for microemulsions.

$$N_{max} = \left\lfloor 0.65 \frac{(R_1+2R_2)^3 - R_1^3}{R_2^3} \right\rfloor \qquad \text{(supplementary equation 4)}$$

The fraction in supplementary equation 4 represents the volume of the spherical shell delimited by the dashed line surrounding the nanoparticle in supplementary figure 1 (having an external radius of R_1+2R_2 and an internal radius of R_1), divided by the volume of an individual spherical protein of radius

R_2. The number 0.65 is an empirical multiplier representing the solid fraction of the spherical shell (F_{solid}) that is the volume fraction effectively occupied by the surrounding spheres and is based on previous observations on microemulsions.

F_{solid} was written as a function of $r=R_2/R_1$ and N calculated from supplementary equation 2 and resulted into supplementary equation 5.

$$F_{solid} = \frac{Nr^2}{2(4r^2+6r+3)} \qquad \text{(supplementary equation 5)}$$

Values of F_{solid} calculated in a broad range of R_2/R_1 are plotted in supplementary figure 6. Using supplementary equation 5, the model described by supplementary equation 4 can be re-written as the more general supplementary equation 6, which is applicable for any $R_2/R_1 \leq 0.6$ and takes into account the solid fraction of spherical shell calculated within the new geometrical model rather than an empirical value determined in another context (light scattering of microemulsions).

$$N_{max} = \left\lfloor F_{solid} \frac{(R_1+2R_2)^3 - R_1^3}{R_2^3} \right\rfloor \qquad \text{(supplementary equation 6)}$$

Supplementary equation 6 can be potentially used in place of equation 1 presented in the Experimental section.

1.2. Binding assay

The determination of the parameters L_{max} and K_D from the binding assay relies on fitting the experimental data to the Hill-Langmuir equation. Generally, this is obtained by titration of the ligand concentration (in this case RBD). However, when the ligand is a protein, the estimation of the parameters would require a broad range of protein concentrations that challenges the accuracy and range of most protein determination methods and also requires large amounts of protein. In contrast, keeping the protein concentration constant and changing the concentration of the nanoparticles, allowed protein determination within a narrow range compatible with conventional assays, while also providing an accurate determination of L_{max} without using large excess of protein. As in this context, the Hill-Langmuir equation presented in the conventional form has two independent variables, [C] and [NP], the equation was rearranged to facilitate non-linear least squares fitting as shown in supplementary equation 7.

$$[C]_{NP} = \frac{[C]_0 + L_{\max[NP]} + K_D - \sqrt{\left([C]_0 + L_{\max[NP]} + K_D\right)^2 - 4[C]_0 L_{\max[NP]}}}{2} \qquad \text{(supplementary equation 7)}$$

As the number of protein molecules per particle N is a more useful estimate of the extent of binding compared to L_{max}, this was calculated with equation 5 (see Experimental section). L_{max} is defined as the ratio between the mass of protein per unit of mass of nanoparticles, which can be described by.

$$L_{max} = \frac{NM_r}{M_{NP}N_A} \qquad \text{(supplementary equation 8)}$$

Here, M_r represents the relative mass of the protein (g mol^{-1}), N_A the Avogadro constant (mol^{-1}) and M_{NP} the mass of a single nanoparticle (g). M_{NP} can be calculated from supplementary equation 9 using the density of the nanoparticle ρ and its volume V_{NP}, assuming spherical shape and radius R_1.

$$M_{NP} = V_{NP}\rho = \frac{4}{3}\pi {R_1}^3 \rho \qquad \text{(supplementary equation 9)}$$

Equation 5 in the Experimental section was obtained by rearranging supplementary equations 8 and 9 and using a 10^{-21} multiplier that takes into account units conversion.

2. Supplementary Figures and Tables

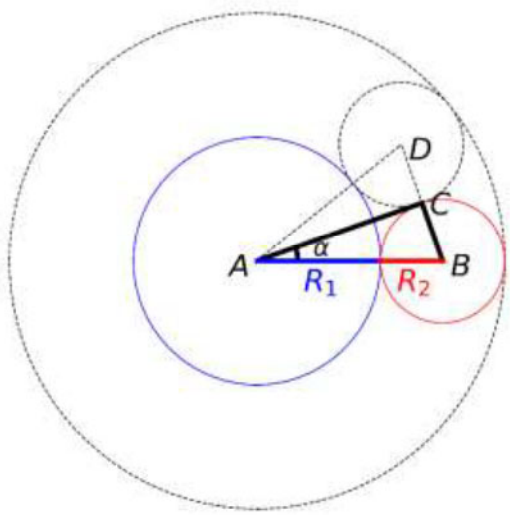

Supplementary Figure 1. Simplified schematic of the geometrical model of spheres packing. The schematic is a 2D representation of the geometry of a spherical nanoparticle of radius R_1 (blue) surrounded by a spherical protein of radius R_2 (red). The points A, B, C and D represent the centre of the nanoparticle, the centre of the spherical protein, the point tangent to an adjacent protein sphere and the centre of that adjacent sphere. The angle α formed by the segments AB and AC of the squared triangle ABC is the half angular distance between the two tangent protein spheres.

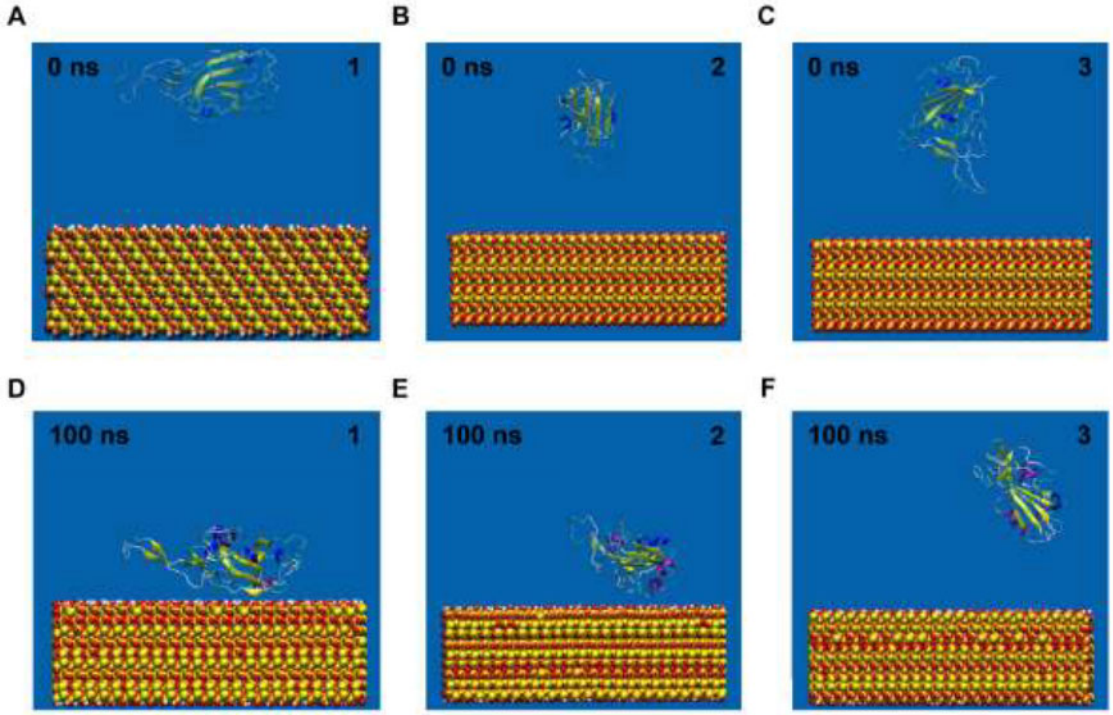

Supplementary Figure 2. Simulation boxes of the three independent MD simulations, showing the initial orientation of the RBD with respect to the silica layer on the bottom of the boxes (A-C) and final configuration at 100 ns (D-E).

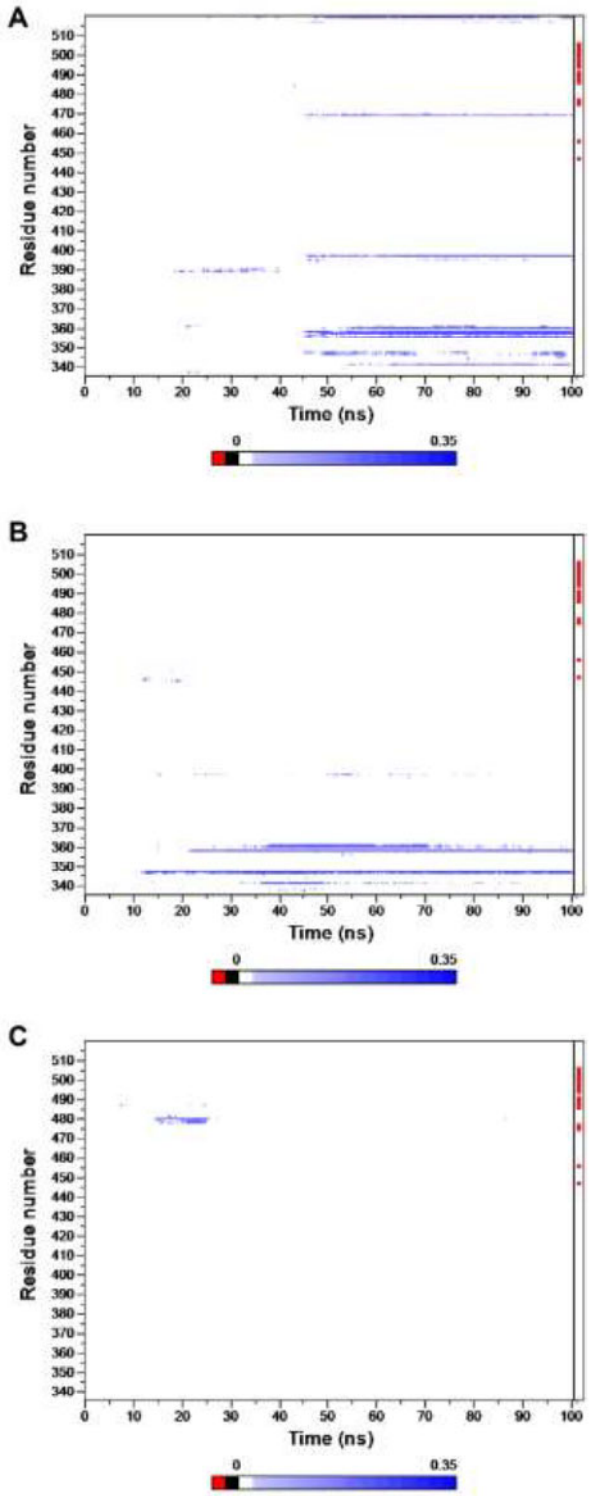

Supplementary Figure 3. Minimum distance from the silica of all RBD residues over time. For each simulation frame, all RBD atoms within 0.6 nm of any oxygen or hydrogen on the silica were considered potential contact atoms. For each residue, the smallest distance between a potential contact atom and silica surface atoms was plotted, resulting in minimum distances less than 0.35 nm. On the right side of the plot, red dots indicate contacts of the RBD with the ACE2 enzyme (from the complex of PDB ID: 6M17).

Residue	Mean contact distance ± SD in simulation 1 (nm)	Mean contact distance ± SD in simulation 2 (nm)
E340	0.26 ± 0.07	0.22 ± 0.06
T345	0.25 ± 0.04	0.26 ± 0.05
R346	0.18 ± 0.01	0.26 ± 0.05
N354	0.21 ± 0.04	
R355	0.31 ± 0.03	
K356	0.17 ± 0.01	
R357	0.18 ± 0.02	0.21 ± 0.03
S359	0.21 ± 0.06	0.22 ± 0.04
N360	0.23 ± 0.05	
Y396	0.22 ± 0.04	
I468	0.25 ± 0.03	
L518	0.23 ± 0.06	

Supplementary Table 1. The 12 amino acids closely interacting with the silica and their mean contact distance from the surface during the simulations. The mean contact distance is computed as the mean over time of the minimum distances plotted in Supplementary Figure 3, with the error representing the standard deviations (SD). Only the amino acids found within contact distance from the surface for a cumulative time longer than 20 ns are included in the table. The residues highlighted in red are those featured in Figure 4B. In simulation 3 the interaction was only transient and none of the amino acids remained within contact distance from the surface for longer than 20 ns.

```
     1          11         21         31         41         51
     |          |          |          |          |          |
  1              SQCVNLTT RTQLPPAYTN SFTRGVYYPD KVFRSSVLHS TQDLFLPFFS    60
 61 NVTWFHAIHV SGTNGTKRFD NPVLPFNDGV YFASTEKSNI IRGWIFGTTL DSKTQSLLIV   120
121 NNATNVVIKV CEFQFCNDPF LGVYYHKNNK SWMESEFRVY SSANNCTFEY VSQPFLMDLE   180
181 GKQGNFKNLR EFVFKNIDGY FKIYSKHTPI NLVRDLPQGF SALEPLVDLP IGINITRFQT   240
241 LLALHRSYLT PGDSSSGWTA GAAAYYVGYL QPRTFLLKYN ENGTITDAVD CALDPLSETK   300
301 CTLKSFTVEK GIYQTSNFRV QPTESIVRFP NITNLCPFGE VFNATRFASV YAWNRKRISN   360
361 CVADYSVLYN SASFSTFKCY GVSPTKLNDL CFTNVYADSF VIRGDEVRQI APGQTGKIAD   420
421 YNYKLPDDFT GCVIAWNSNN LDSKVGGNYN YLYRLFRKSN LKPFERDIST EIYQAGSTPC   480
481 NGVEGFNCYF PLQSYGFQPT NGVGYQPYRV VVLSFELLHA PATVCGPKKS TNLVKNKCVN   540
541 FNFNGLTGTG VLTESNKKFL PFQQFGRDIA DTTDAVRDPQ TLEILDITPC SFGGVSVITP   600
601 GTNTSNQVAV LYQDVNCTEV PVAIHADQLT PTWRVYSTGS NVFQTRAGCL IGAEHVNNSY   660
661 ECDIPIGAGI CASYQTQTNS PRRAR
```

Supplementary Figure 4. Spike protein S1 sequence (amino acids 13-685 of UniProt KB entry P0DTC2). Residues with the grey background represent the RBD (amino acids 319-541), whereas underlined amino acids are from the structure used in the MD simulation (PDB ID: 6M17). Residues with pink background are those involved in the binding to ACE2 whereas the yellow background highlights amino acids which stayed in contact with the silica layer for longer than 20 ns.

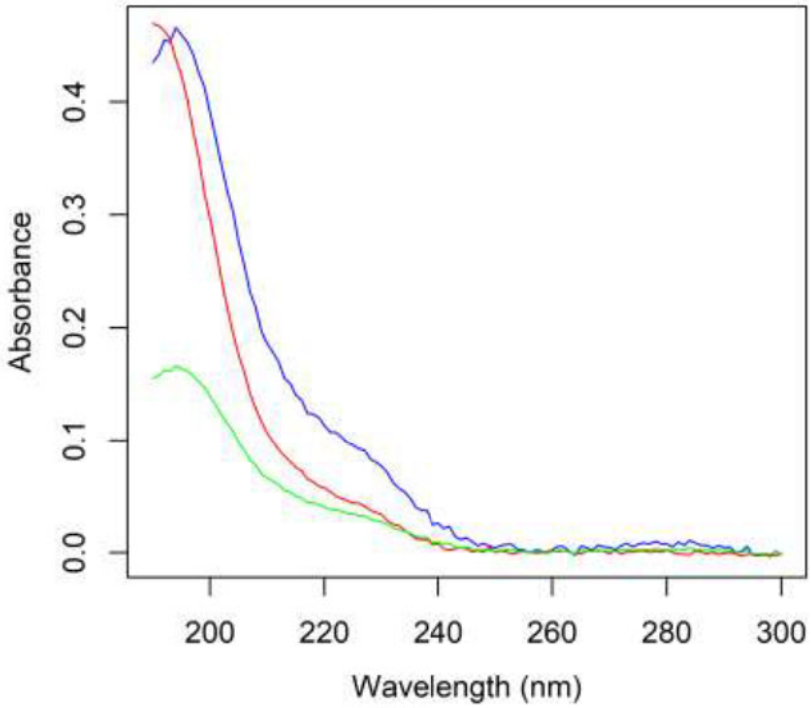

Supplementary Figure 5. UV extinction spectra of RBD in solution (red), bound RBD (green) and bound RBD normalised to the concentration of RBD in solution (blue). The spectrum of bound RBS was obtained from the light scattering-corrected subtraction of RBD extinction spectra before and after nanoparticle removal by centrifugation.

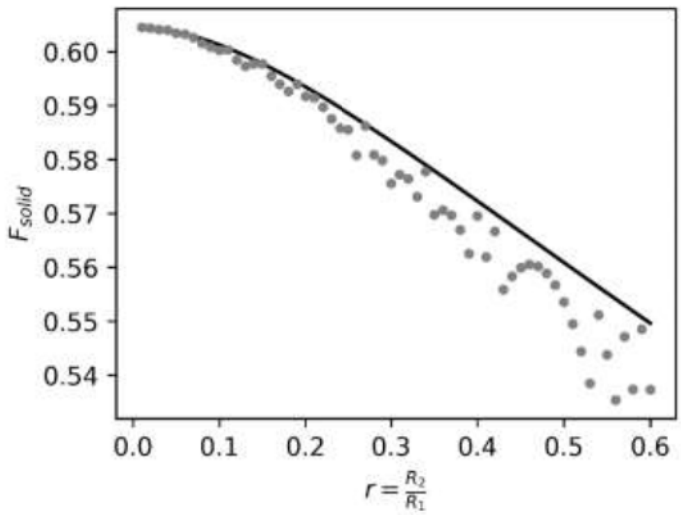

Supplementary Figure 6. Fraction of the spherical shell surrounding a nanoparticle occupied by spherical proteins. F_{solid} is plotted as a function of $r=R_2/R_1$ and spans from 0.54 to 0.60 for values of r of 0.6 and 0.1 respectively. A variable F_{solid} is in contrast to a previously reported model where a constant value F_{solid} = 0.65 was adopted from empirical observations on microemulsions. Grey dots represent values of F_{solid} calculated using supplementary equation 5 and N as positive integer numbers. To highlight the trend of F_{solid} better, the black line was calculated by omitting the floor function from supplementary equation 2, thus yielding any positive N in a continuous way. The comparison between the black continuous line and the F_{solid} calculated for finite numbers (grey points) shows that the continuous function describes the solid fraction well only when the surrounding spheres are substantially smaller than the nanoparticle (very small r). Instead, when the size of the nanoparticle is closer to the size of the surrounding spheres (larger r), which is the case in many studies of proteins adsorption on nanoparticles, the solid fraction does not follow the continuous trend closely.